Archives of Civil and Mechanical Engineering (2023) 23:198
https://doi.org/10.1007/s43452-023-00741-4

ORIGINAL ARTICLE

Effect of crack angle and concrete strength on the dynamic fracture behavior of rock-based layered material containing a pre-existing crack

Tengfei Guo[1] · Kewei Liu[1] · Xiang Li[2] · Peng Jin[1] · Jiacai Yang[1] · Aimin Zhang[1] · Liansong Zou[1]

Received: 9 May 2023 / Revised: 26 June 2023 / Accepted: 2 July 2023 / Published online: 12 July 2023

Abstract
Dynamic fracture behavior of rock-based layered material containing a pre-existing crack was investigated, which is crucial to evaluate the stability of rock-based systems. Dynamic tests on semi-circular bend (SCB) samples were conducted with a split-Hopkinson Pressure Bar (SHPB) system and the cracking process was collected using digital image correlation (DIC). An MTS Insight 30 electromechanical test equipment was adopted to perform static fracture experiment for comparison. Different typical fracture modes were classified: interfacial fracture, combined mode of tensile–shear fracture, and combined mode of compression–shear fracture. Regardless of static load or dynamic load, the fracture mode is controlled by crack dip angle, and the peak load is proportional to crack dip angle. The increase in concrete strength makes a strengthening impact on the bearing capacity of SCB sample, which can prevent the propagation of secondary cracks in the concrete. Both static and dynamic fracture toughness are significantly affected by dip angle. The difference between static and dynamic fracture toughness of mixed-mode reduces initially and subsequently increases with an increase in dip angle. Furthermore, comparing with static fracture toughness, dynamic fracture toughness substantially depends stronger on dip angle. The dip angle and concrete strength have an obvious effect on the fracture resistance.

Keywords Rock-based layered sample · SCB · Concrete strength · Propagation behavior · Fracture toughness

1 Introduction

Rock-based layered structures are frequently utilized in engineering construction projects, including tunneling, civil engineering, and mining. Examples include surrounding rock-shotcrete/rock-lined structures, concrete gravity dams, and cement paste backfill (CPB) structures [1–6]. Barrett et al. [1] proposed four deterministic design models for the shotcrete surrounding rock structure. Based on these models, studies show that adhesion is crucial for the support ability of shotcrete, but after the peak, flexural strength and toughness play a controlling role. Johnston et al. [2] investigated the interface shear behavior between concrete and rock in bored piles and found that the lateral shear performance was determined by the shear properties of the rough interface between concrete and rock. Ulfberg et al. [3] investigated the effect of concrete material parameters on the ultimate bearing capacity of a scale model dam based on scale model tests. The results indicate that the material parameters of concrete play a vital role in the load-bearing capacity of the dam when there is a significant geometric change in the concrete–rock dam foundation interface. Fishman et al. [4] explained the fracture mechanism of concrete structures on rock foundations under compression–shear conditions through experimental analysis. Alneasan et al. [5] studied inclination interface crack between two dissimilar rock layers, revealing that the extension path of interface crack is determined by the elastic stiffness ratio of two rock layers and crack dip angle. Huang et al. [6] conducted an experimental study for CPB-rock structures and found that different binder types and contents have significant effects on

✉ Kewei Liu
kewei_liu@csu.edu.cn

✉ Xiang Li
lixiang85@mail.sysu.edu.cn

[1] School of Resources and Safety Engineering, Central South University, 932 South Lushan Road, Changsha 410083, China

[2] School of Civil Engineering, Sun Yat-sen University, Zhuhai 519082, China

mode I fracture toughness of interface. Interfaces and bedrock flaws at various scales may exist in rock-based structures. The interface between the two materials is a weak point in rock-based layered system, and flaws in the rock could cause a hidden threat to the stability of layered structure, which will lead to the weakening of the disaster resistance of the overall structure. Furthermore, the layered material is highly prone to disasters due to the influence of human activities and geological environment variables [7–13]. For example, Sujatha et al. [7] pointed out that the interface will aggravate the crack extension under load, and based on the fracture mechanics method, a friction model considering the interaction between interface was proposed. Fishman et al. [8] discussed the damage mechanism of rock–concrete structures and proposed a practical method for studying the ultimate turning resistance of structures. According to a modified interface cracking model, the stress intensity factor in different materials was obtained [9, 10]. Zhou et al. [11, 12] found that fractures and joints have an essential influence on the overall fracture characteristics of surrounding rock, and elucidated their relationship with the fracture behavior of material. Meng et al. [13] experimentally investigated the influences of bedding plane and fracture angle on the cracking behavior of layered materials in mixed mode, and revealed the fracture mechanism of layered material. Thus, a comprehensive understanding of the fracture propagation behavior and fracture characteristics for rock-based bi-material systems with cracks of varying dip angles is critical to assessing the overall stability.

Research scholars on the fracture characteristics of rock–concrete have conducted plenty of work in terms of experiments, numerical simulations, and theoretical analysis, where three-point bending (TPB) tests and four-point bending (FPB) methods [14–17] are usually used. For example, the evolution of fractures in layered rock was investigated through TPB experiments, revealing the mechanism of fracture penetration/deflection of layered planes [14, 15]. Luo et al. [16] presented a method through TPB experiments to quantify the energy at material failure. Marsavina et al. [17] elucidated the mechanism of interface crack extension in bi-material samples via FPB experiments. Charalambides et al. [18] investigated the interface fracture characteristics based on the FPB test method. Suo and Hutchinson [19] presented a sandwich configuration sample and reported cracking behavior for interface crack. Lee and Buyukozturk [20] also analyzed the fracture characteristics of bi-material interface with FPB tests using sandwich samples. Buyukozturk and Hearing [21] reported cracking in the interfacial region of two-phase composites and parameters affecting the fracture behavior of concrete by TPB experiments. Agrawal et al. [22] demonstrated that the interface fracture characteristics of aluminum–vinyl ester bi-material samples were controlled by the mode mixing ratio based on FPB experiments. Yang et al. [23] investigate the fracture characteristics of the rock–concrete using different fracture modal mixtures in terms of TPB and FPB tests. Zhong Hong et al. [24] analyzed the relationship between cracking behavior of bi-material and modal mixing ratio using an FPB method. Chen et al. [25] performed TPB experiments to verify the fracture toughness of materials obtained from the wedge splitting model. Guan et al. [26–28] proposed a simple closed-form solution and a simplified two-point method that can be utilized to obtain fracture toughness through a series of TPB and FPB experiments. Dong Wei et al. [29–31] conducted TPB and FPB tests on rock–concrete layered samples with various interface roughness, presented a cracking criterion for rock–concrete interface, and calculated related mechanical parameters. These studies are undoubtedly conducive to understanding the fracture characteristics of rock–concrete systems and are crucial in improving the construction quality and safety of rock foundation systems. It is worth noting that the above bending tests are inappropriate for beam members containing weak interfaces, because such beam samples may crack or even break prematurely under their high self-weight. Therefore, an SCB method was further proposed and recommended as a standard approach to structural fracture research [32]. This type of configuration sample has several strengths over other samples, including cost-effectiveness, convenience processing and testing procedures, and universal testing device requirements. Moreover, by introducing cracks at various angles in SCB configuration samples, the cracks can experience a variety of stress states, and then realize modes including tension, shear, and combination mode. Hence, the SCB test approach is frequently utilized to investigate the flaw growth behavior and fracture toughness of laminated medium [33–38]. Scholars used SCB samples to detailedly investigate the influence of loading conditions, mechanical characteristics, and bedding structure on the fracture behavior of layered media. The above studies indicated that mechanical behavior is significantly affected by bedding strength and loading direction, in which propagation path and fracture toughness are determined from loading direction [33–35]. Nejati et al. [36] proposed an improved SCB test method for layered rocks, which presents the relationship between different anisotropy ratios and orientations and normalized stress intensity factors. The primary purpose of the above studies, however, is to study the effect of various bedding structure parameters on fracture behavior of layered media. Recently, Huang and Fang et al. [6, 37, 38] used SCB samples to analyze the fracture characteristics of CPB–rock structure, which revealed that the fracture behavior of composite structures was determined by cementing materials, environmental variables, and loading methods.

The above studies are conducive to clearly understanding of the mechanical characteristics of composite structures under static loading. For concrete construction projects on

practical rock foundations, structure-rock foundation system are more susceptible to dynamic disturbances, which include hydrodynamic loads on concrete hydraulic dam foundations, oscillation of vehicles driving on tunnels and roadbeds and impact loads such as blasting and rock bursts in underground tunnel construction. Investigation on rock/concrete fracture mechanics under dynamic loads has always been a hot topic, and researchers have conducted many experiments and achieved important research results [39–44]. Unfortunately, the lack of studies on the mechanical characteristics of cracked combined structures under dynamic conditions limited our understanding of the cracking behavior of this structure type. Recently, Qiu Hao et al. [45, 46] studied dynamic crack extension behavior and failure path of rock-mortar samples under dynamic conditions. Research shows that interface roughness and impact speed obviously influence the crack propagation path and composite fracture toughness of composite structures. Focusing on the influence of interface crack tip position and related parameters, Sundaram et al. [47] analyzed fracture characteristics of layer structures, and explained the crack penetration-branching mechanism. Their results showed that the crack angle plays a significant role in interfacial crack growth and fracture toughness.

These basic studies are significantly beneficial to understand the fracture mechanism of rock-based layered systems, which is important for improving its security and durability. In practical construction projects, the rock foundation may have several natural flaws and form arbitrary angles with the interface. Since the crack–interface interaction, the fracture characteristics of rock-based layered system are particularly complicated and depend on the combined effect of interface properties and its whole behaviors. Although scholars have struggled to investigate the interface cracking of composite structures, they have mainly focused on interface cracking behavior, with a few studies focused on crack–interface interaction; thus, our knowledge of the stability of layered structures is limited. To overcome this issue, the current study performed experiments on rock-based layered SCB samples that adopted the Split Hopkinson Pressure Bar (SHPB) test system, with the high-speed camera device being utilized to monitor the fracturing process. The cracking behavior under various dip angles and concrete strength is analyzed. Furthermore, the stress intensity factors of rock-based layered SCB samples were solved utilizing ABAQUS software, and the effects of varied crack dip angle and concrete strength on its fracture toughness were investigated. Static tests were then performed on rock–concrete samples utilizing an MTS Insight 30 electromechanical control test system for comparison.

2 Experimental methods

2.1 Sample and test procedure

Figure 1 depicts the overall process for preparing rock-based layered SCB samples. The specific preparation method is as follows. Natural sandstone blocks without obvious fissures were made into sandstone plates with

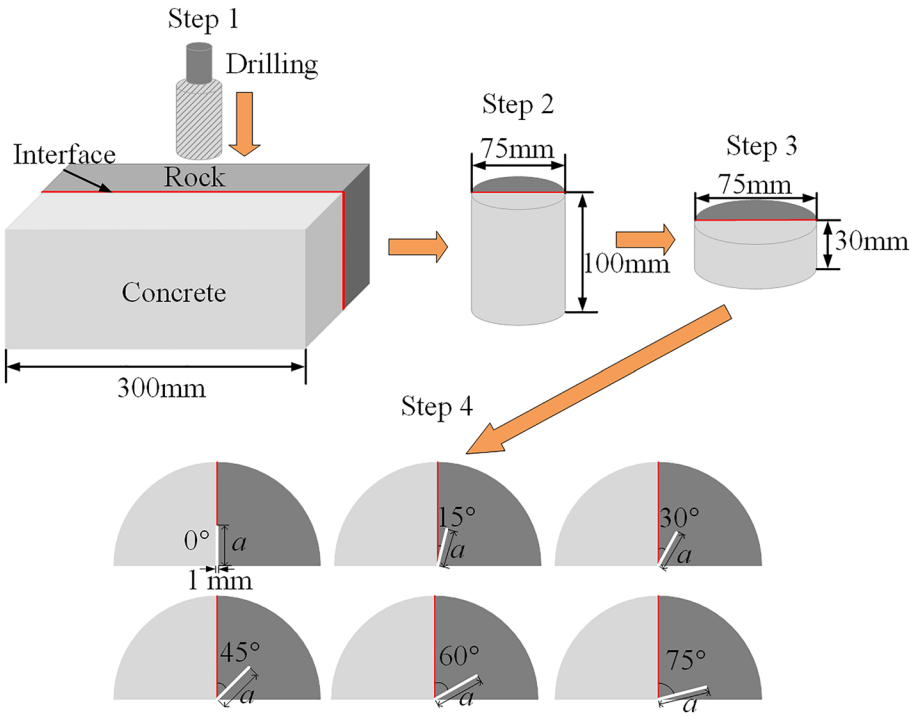

Fig. 1 Preparation process for rock-based layered SCB sample

dimensions of 300 mm × 110 mm × 50 mm, and artificial grooves with dimensions of 1.8 mm × 1.4 mm × 2.2 mm (depth × width × spacing) were cut on the surface of the slabs for roughening to promote interfacial adhesion. The sandstone slab was then placed in a mold, which is full of 40 mm of thick concrete. Then, it was cured in a standard curing room for 28 days under the same room temperature and humidity, the disc samples with diameter (D) and thickness (B) of 75 mm and 30 mm were machined. In this process, dimensional errors of each disc were carefully restricted within ± 0.5 mm, and flatness of both end surfaces was strictly controlled within ± 0.1 mm. Finally, the SCB sample was obtained by cutting the disc in half, and a crack of $2a$ ($a = 16$ mm) in length and 1 mm in width (t) was created in SCB sample utilizing a precision cutting device. Six pre-existing cracks ($\theta = 0°$, 15°, 30°, 45°, 60°, and 75°) were selected to analyze the impact of cracks on fracture characteristics of SCB samples in detail (Fig. 1). The span denoted by 2S, between the two bearings measures 37.5 mm (Fig. 2).

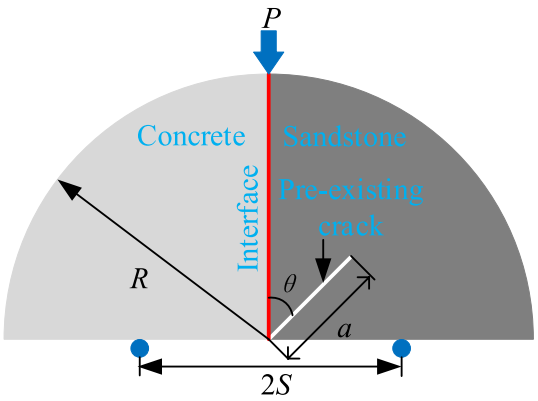

Fig. 2 Schematic diagram of layered sample for SCB test

There were 72 samples used in this study, 18 were subjected to static load testing, and the remaining 54 were subjected to dynamic load testing. The geometry of test samples as well as the average experiment results is presented in Table 1. The samples' numbers are *S*-θ, where *S* stands for the static condition and θ stands for the angle of pre-existing crack to interface. Likewise, for samples marked *DC*-θ, *D* is dynamic conditions, *C* stands for *A*, *B*, or *C*, denoting various concrete strength of SCB samples, and θ denotes the angle of pre-existing crack to interface.

To effectively use the experiment findings to evaluate the stability and durability of rock-based structures in practice, black sandstone rock masses with no obvious fractures were chosen in the field, and concrete materials were used to conduct laboratory experiments of layered structures.

Table 1 Basic parameters and mechanical properties

Loading condition	Sample number	θ	D (mm)	B (mm)	$2a/t$ (mm/mm)	Peak force (kN)
Static	*S*-0	0°	75.08	30.03	16.06/0.96	2.23
	S-15	15°	74.95	29.92	16.02/0.97	2.51
	S-30	30°	75.04	30.08	15.96/0.95	2.78
	S-45	45°	75.03	29.95	16.02/1.07	3.46
	S-60	60°	74.91	30.03	16.03/0.95	4.25
	S-75	75°	75.02	29.98	15.98/1.03	6.15
Dynamic	*DA*-0	0°	74.97	30.09	16.02/0.98	12.67
	DA-15	15°	75.06	29.92	16.03/0.98	13.44
	DA-30	30°	75.03	30.06	15.96/0.96	15.11
	DA-45	45°	74.96	30.02	16.03/1.06	18.3
	DA-60	60°	75.02	29.98	16.06/0.97	21.28
	DA-75	75°	74.98	29.97	15.98/1.02	31.26
	DB-0	0°	75.02	30.01	16.05/0.98	13.48
	DB-15	15°	75.03	29.95	16.02/0.98	14.89
	DB-30	30°	74.92	30.02	15.98/0.98	16.07
	DB-45	45°	75.06	29.96	15.95/1.02	20.05
	DB-60	60°	74.96	30.05	16.02/0.98	23.75
	DB-75	75°	75.03	29.96	16.06/1.03	35.62
	DC-0	0°	75.09	30.06	16.02/0.97	16.21
	DC-15	15°	75.03	30.02	15.98/1.03	17.23
	DC-30	30°	74.98	30.05	15.95/0.96	18.72
	DC-45	45°	75.02	30.06	16.03/0.99	22.86
	DC-60	60°	74.98	29.94	16.02/1.03	26.71
	DC-75	75°	75.04	29.92	15.95/0.98	38.01

Figure 3 illustrates the sand particle-size gradation curves. Three various mix proportions of concrete were adopted, with mass ratios of cement, sand, and water of 1.0:2.1:0.5, 1.0:1.6:0.4, and 1.0:1.0:0.35, respectively. The material properties of sandstone and concrete are listed in Table 2. Among them, the dynamic tensile strength was obtained by conducting SHPB tests on rock and concrete Brazilian disc samples (with diameter of 50 mm and thickness of 25 mm) prepared in the laboratory.

2.2 Testing apparatus and procedure

2.2.1 Test setups

Static SCB tests were conducted with a 30 kN MTS Insight 30 system, as presented in Fig. 4. The sample was supported on a loading plate by two steel round bars (3 mm in diameter). The current tests were conducted adopting displacement control (0.02 mm/min) method. The displacement and load in the vertical direction of the sample were measured by a high-precision (0.001 mm) linear variable differential transformer and an electronic load transducer (load accuracy: ± 0.5%), respectively.

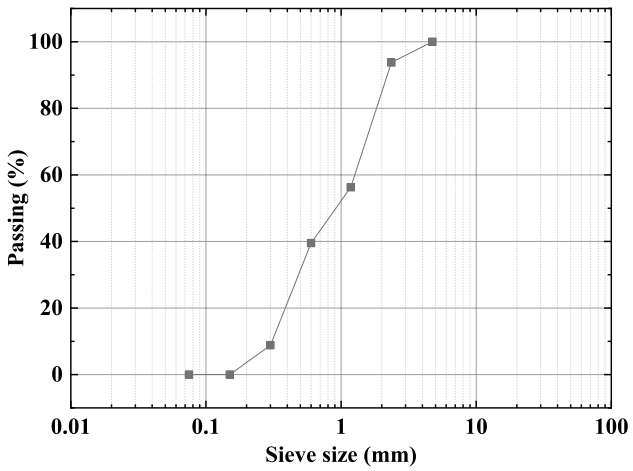

Fig. 3 Grading curves of sand

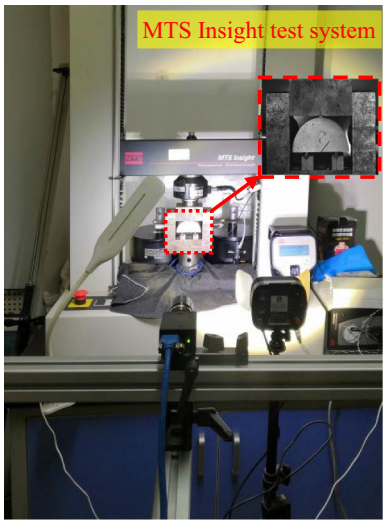

Fig. 4 Static SCB tests. *LS* low speed

Figure 5a indicates that an SHPB system was employed for the dynamic SCB testing, which included a bullet-shaped striker, incident and transmitted bar, and a buffered bar. Many investigations have proven that mechanical behavior is significantly affected by the friction between bars and sample end face [48–50]. As a result, petroleum jelly is necessary to uniformly coat the loading end of the SCB sample to decrease the frictional effect. By opening the gas valve, the conical strikers are launched from the pressure vessel and strike the right side of incident bar, generating a half-sine wave that passes on incidence bar to sample, as shown in Fig. 5b. There are two types of waves that can result from an incident wave reaching a sample: the reflected wave and transmitted wave. The three waves were captured using two strain gauges and recorded with a digital oscilloscope.

2.2.2 DIC technique

The fracture processes of layered SCB samples under static conditions were obtained using a low-speed photography system. Figure 4 presents the primary components of the low-speed photography equipment, namely a camera

Table 2 Material properties

Items	Density (kg/m^3)	Principal wave velocity (m/s)	Young's modulus (GPa)	Poisson's ratio	Uniaxial compressive strength (MPa)	Static tensile strength (MPa)	Dynamic tensile strength (MPa)
Rock	2520.23	3121.26	12.40	0.302	70.12	2.88	20.52
Concrete							
Mix-1	2081.32	2588.62	10.36	0.164	44.25	2.72	17.31
Mix-2	2104.26	2684.28	12.32	0.188	66.68	2.85	19.15
Mix-3	2178.64	2868.52	16.71	0.173	81.43	3.16	21.92

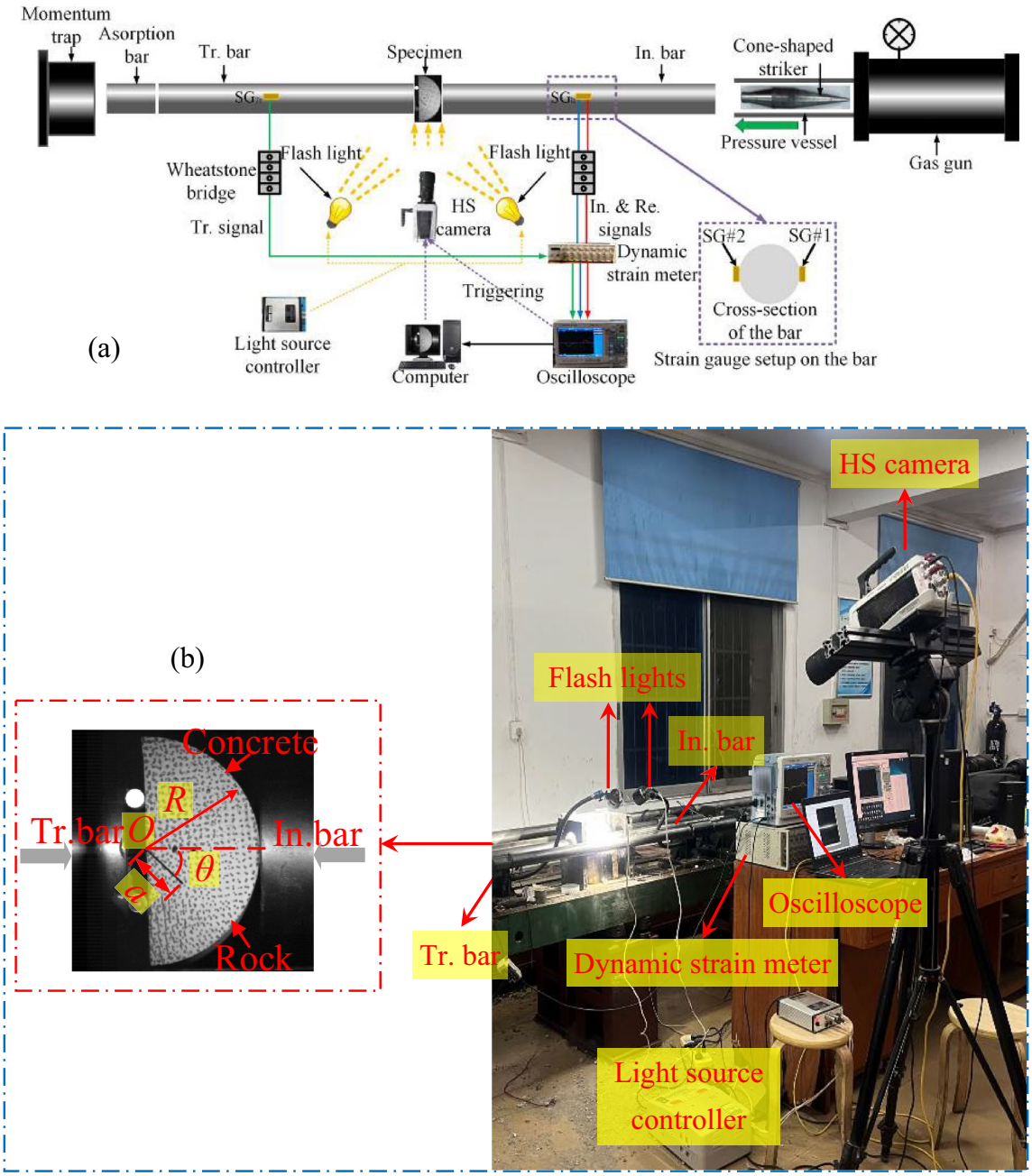

Fig. 5 Dynamic SCB tests: **a** schematic diagram; **b** loading equipment. *HS* high-speed, *In* incident, *Tr* transmission, *Re* reflection, *SG* strain gauge

including an image sensor and two LED flashes (ZF-3000). The two LED flashlights were placed in front of the sample for illumination. An LS camera with a resolution of 4096 × 3000 pixels is adopted, and the frame rate was set to 15 fps (frames per second), which can effectively capture the fracture propagation process.

In the dynamic test, the HS camera device was adopted to capture the dynamic fracture process simultaneously. Two LED flashlights were lighted on the surface of samples, and the HS equipment (Vision Research Inc.—Phantom V711) with a resolution setting of 256 × 256 pixels and an inter-frame time of 12.6 μs was used to capture the dynamic cracking and expansion process, as shown in Fig. 5. When the voltage value measured via SG is greater than − 34 mV, and then, oscilloscope releases a transistor–transistor logic pulse to trigger the HS equipment, which automatically records the complete deformation image of the sample.

The DIC method can efficiently record strain field and deformation path data on the surface of material and is extensively used for the investigation of the fracture characteristics of objects [11, 51, 52]. It was employed to collect deformation field information image of rock-based layered material in the current investigation. Then, the DIC post-processing calculations were performed in the MATLAB environment using the Ncorr [53] program. This program was primarily derived from Pan's reliability-guided DIC approach [54]. The computational procedure is shown below: (1) Set an initial image as a reference and then select target images; (2) introduce the semi-circular region of interest (ROI); (3) calculate the final displacement; (4) obtain the strain field information.

2.2.3 Test scheme

To thoroughly study the impact of crack dip on the cracking behavior of layered structures under dynamic and static conditions, dynamic and static experiments were conducted on SCB samples with six prefabricated crack dips, respectively, as illustrated in Fig. 1. In addition, three different concrete strengths were considered in dynamic testing to assess the effect of bi-material strength ratio on the dynamic fracture characteristics of SCB samples. In the current work, tests were repeated three times for each dip angle and concrete strength to assure the validity of results. The SCB samples were placed on a loading frame with two supports, and the LS photography device was debugged to maintain acquisition synchronization with the MTS loading device (Fig. 4). The SCB samples were then placed between the incident and transmitted bars in the dynamic test, and data were collected using the HS camera equipment in synchronization with the SHPB load device.

2.3 Testing principle

Dynamic balance was thoroughly checked for all dynamic test samples to assure data validity. Figure 6 shows the dynamic balance of a typical SCB sample. In Fig. 6a, the strain gauge monitors the initial pulse signal under dynamic load. Figure 6b indicates that the dynamic pressure P_1 (pressure at the incidence end) and P_2 (pressure at the transmission end) at both ends of sample are basically similar. According to the aforementioned findings, the dynamic balance requirement is satisfied under dynamic loading, indicating that the inertial effect can be ignored, since the force differential that creates is negligible in the sample [55].

The dynamic force P_1 and displacement u_1 at the incident bar–sample interface, and dynamic force P_2 and displacement u_2 at the transmitted bar–sample interface are obtained using the following expressions, derived from one-dimensional stress wave theory [56]:

$$P_1 = EA\left[\varepsilon_i(t) + \varepsilon_r(t)\right], P_2 = EA\varepsilon_t(t) \tag{1}$$

$$u_1 = C_b \int_0^t \left[\varepsilon_i(t) - \varepsilon_r(t)\right] \mathrm{d}t, u_2 = C_b \int_0^t \varepsilon_t(t)\, \mathrm{d}t. \tag{2}$$

In these equations, A, E, and C_b refer to the bar cross-sectional area, Young's modulus, and elastic wave velocity, respectively, and $\varepsilon_i(t)$, $\varepsilon_r(t)$, and $\varepsilon_t(t)$ denotes the incident strain, reflected strain, and transmitted strain, respectively.

After verifying in strict dynamic equilibrium, the average force and relative displacement δ(t) of the sample can be obtained by

$$\overline{P}(t) = \frac{1}{2}\left[P_1(t) + P_2(t)\right], \delta(t) = u_1(t) - u_2(t). \tag{3}$$

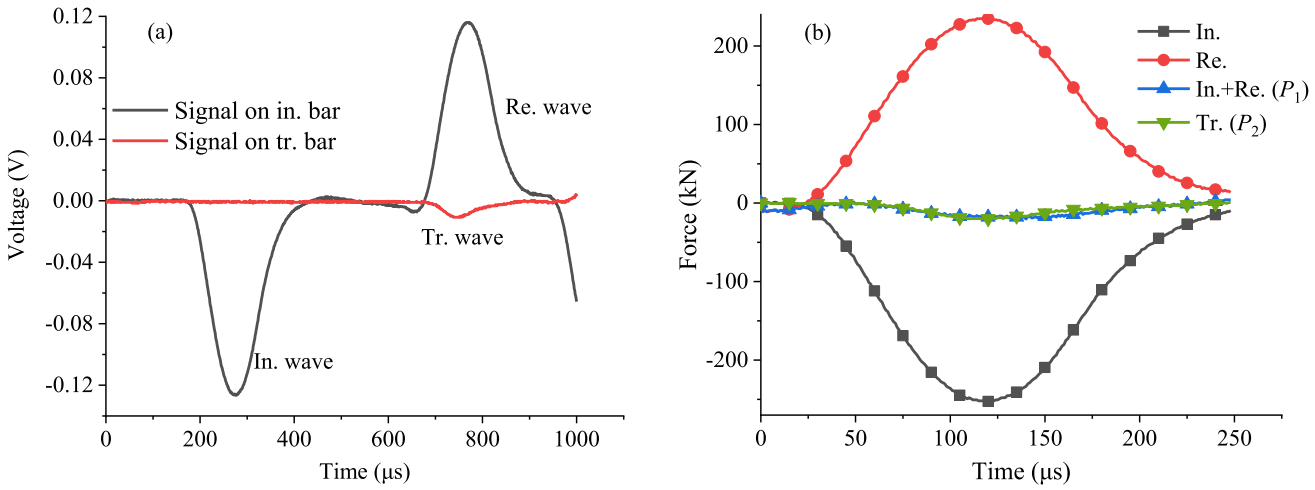

Fig. 6 Dynamic force history in SCB tests: **a** original signal and **b** dynamic force balance

3 Test results

3.1 Fracture behavior analysis

3.1.1 Fracture process

The crack dip angle under static and dynamic loading has an important impact on the development process and propagation path of the sample. Given that development procedures under static and dynamic loading possess similarity, this study takes the fracture development process under dynamic loading as an example. Furthermore, high-speed camera and DIC were utilized to analyze the dynamics of vertical strain ε_{yy}, horizontal displacement u_x and vertical displacement u_y in SCB samples over time. Figure 7a–g presents the characteristic images corresponding to the typical time of crack development process for samples with various crack dip angles, containing original failure images, and evolutions of strain and displacement. In Fig. 7, different-colored bars represent different sizes of ε_{yy}, u_x, and u_y for layered SCB samples. It is positive for line strain elongation among them (under tensile stress). Positive values for a displacement field are along the positive axis, whereas negative values represent the opposite displacement.

At the start of the loading (0 μs), there are no noticeable strains or displacements in the sample. Figure 7a presents the crack development of SCB sample at $\theta = 0°$. It is observable that ε_{yy} occurs in the region near the crack tip when interface crack initiates at the pre-existing crack tip (75.6 μs). Then, a secondary crack occurs in the concrete (100.8 μs). Subsequently, a new secondary crack appeared in the rock (176.4 μs), and coalescence formation along the interface led to sample failure.

The wing crack initiates first (88.2 μs) at the pre-crack tip, and ε_{yy}, u_x, and u_y increase significantly near the crack tip when $\theta = 15°$ (Fig. 7b). Then, it develops along the direction of the loading end on the right (113.4 μs), and secondary cracks appear in the concrete. As the time reaches to 151.2 μs, the wing crack coalescence occurs at the loading end on the right side, and the strain field and displacement field change significantly.

The failure modes of SCB samples with $\theta = 30°$ and 45° are illustrated in Fig. 7c, d, which are comparable to the sample with $\theta = 15°$. The primary distinction between these two cases refers to the moment of wing crack emergence and coalescence. Notably, the new crack starts from the deviation of crack tip for SCB samples with $\theta = 60°$ and 75°, and ε_{yy} is formed in the area away from the crack tip; following that, it develops toward interface, and eventually propagates to the right load end. Moreover, the development length of wing crack and the distance between crack

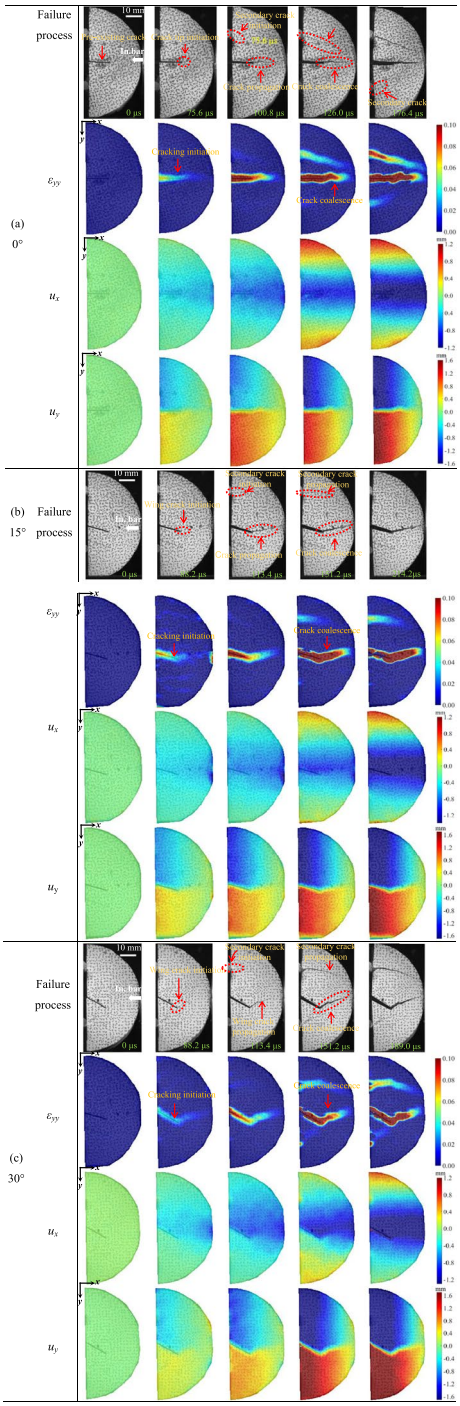

Fig. 7 Fracture process of layered SCB sample under dynamic load conditions

origination location and crack tip both increase with an increase in dip angle. In addition, pre-existing cracks of SCB samples slowly close with increasing dip angle, indicating that the fracture mode of SCB samples has shifted from combined tensile–shear fracture to combined compression–shear fracture.

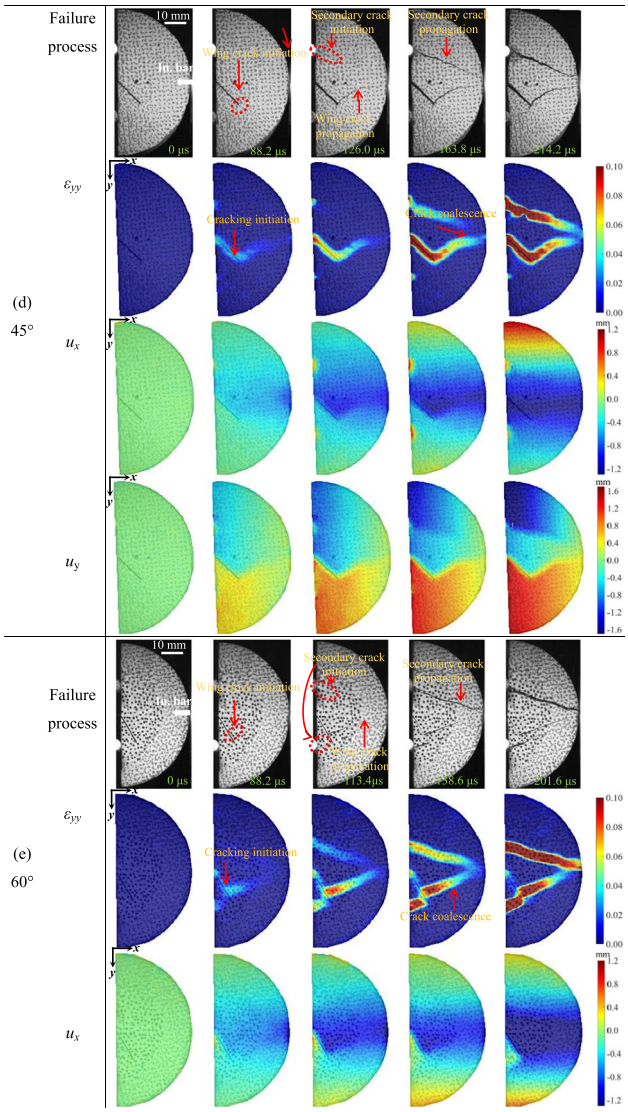

Fig. 7 (continued)

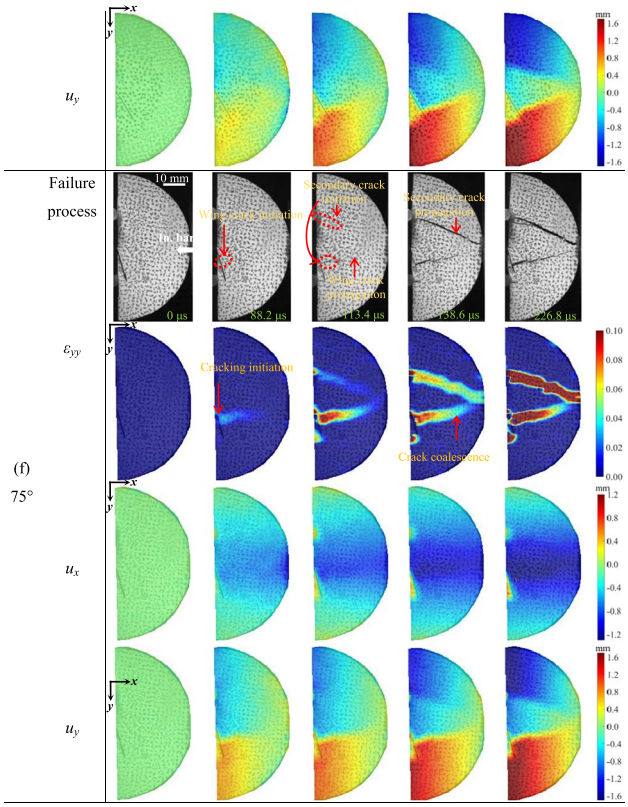

Fig. 7 (continued)

3.1.2 Failure pattern

The impacts of concrete strength and crack dip on failure results for SCB samples in the current dynamic test are illustrated in Fig. 8. The fracture patterns of the samples, which contain three strength ratios of SCB samples, are basically similar. However, due to the difference in concrete strength, the location and quantity of secondary cracks are various, and the secondary crack extension length of the concrete is weakened when the concrete strength is relatively large. The increase in concrete strength leads to a reduction in the length of cracks that develops along the interface, which has an impact on the crack development path. In the previous studies [57], it was found that interface strength plays a critical role in the crack propagation path. When the interface strength is low, interface crack generally appear in SCB sample. The length of interface crack gradually reduces with increasing interface strength, and wing cracks develop. It is noteworthy that when the dip angle is larger (60° and 75°), cracks start far away from the tip. Additionally, the expansion direction of wing cracks is controlled by the dip angle.

Figure 9 shows the fracture propagation paths of SCB samples with different crack dip angles under dynamic and static loading. Figure 9a and Fig. 9b indicate that when $\theta = 0°$, new cracks appear at the tip of pre-cracked, and then develop along the interface, that is, tensile fracture (interfacial fracture) occurs in the sample. For the samples with $\theta = 15°$, 30° and 45°, a wing crack appears at the crack tip and extends to interface along the load direction, and the SCB sample undergoes a combined tensile–shear fracture. New cracks start from the deviation of crack tip as the dip angle increases further (60° and 75°). Then, it propagates toward interface and extends to right loading end eventually, and the sample undergoes compression–shear failure. Further analyzing the cases $\theta = 60°$ and 75°, it is revealed that the deviation between crack initiation position and crack tip increases with increasing dip angle. Notably, the pre-cracked is open at $\theta = 0°$, 15°,30° and 45°, while the pre-cracked is closed at $\theta = 60°$ and 75°. The above observations show that the crack dip angle made an important impact on the fracture modes of layered SCB sample. The tensile fracture mainly

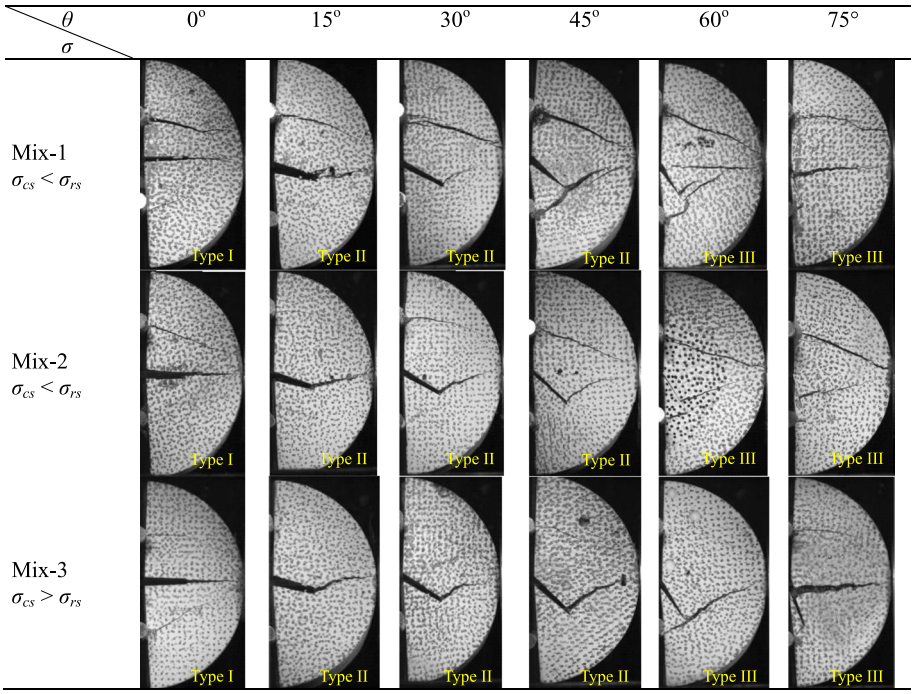

Fig. 8 Effects of concrete strength. σ_{cs} concrete strength, σ_{rs} rock strength

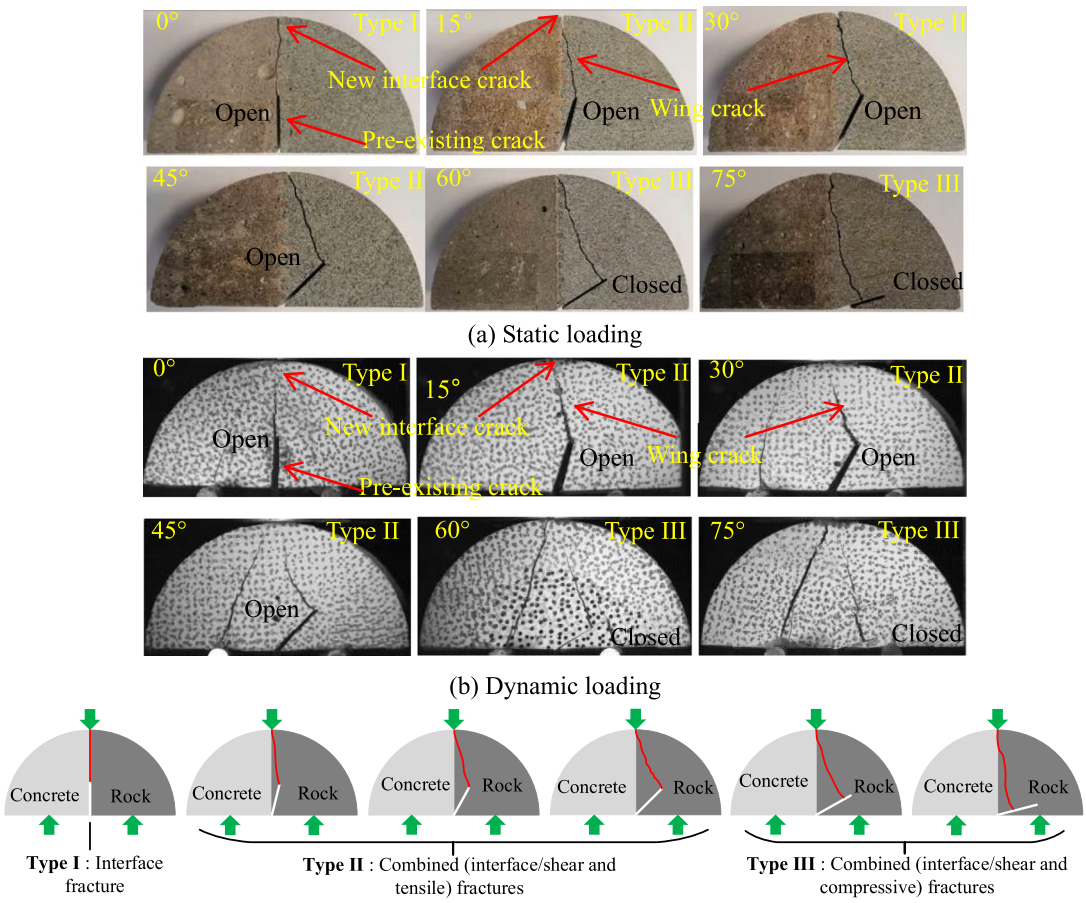

Fig. 9 Effect of dip angle on failure pattern

emerges along interface when the dip angle is low. As the dip angle increases to a certain value, a combined shear and tension fracture is formed, and the sample undergoes a combined compression–shear fracture along the loading direction as the dip angle ulteriorly increases.

Based on the results of sample failure, the three fracture modes are classified below (Fig. 9c):

1. The fracture that develops along the interface is called interface fracture (tensile fracture).
2. The fracture which originates from the tip of pre-existing crack, then extends along the loading direction to the interface, and finally develops to the loading end is called combined fracture (combined tensile–shear).
3. The fracture that initiates far away from the crack tip, then develops to the interface, and eventually propagates to the loading end is known as combined fracture (combined compression–shear).

3.2 Deformation response and peak load

Figure 10a clearly presents static load–displacement curves of samples at various crack dip angles. Early in this loading process, the curve presents nonlinear variation, which is due to the pores and microcracks inside the samples. The microcracks in the sample gradually develop with increasing the load, and the curve shows linear elastic change. After reaching the peak, the primary crack penetrates the sample, and the curve decreases rapidly. It can be seen that the peak load increases gradually when crack dip angle varies from 0° to 75°. The findings suggest that the peak load of SCB sample is highly affected by the crack dip angle. It is further verified that both the peak load and displacement are maximum at $\theta = 75°$, indicating that the crack dip angle determines the deformation of SCB samples [58].

Figure 10b presents dynamic load–displacement curves of SCB samples at various crack dip angles. The cumulative deformation prior to failure is utilized to determine the displacement corresponding to peak load. The incident energy of the sample before the peak load will be converted into its deformation energy in accordance with the principle of energy conservation. The deformation energy is subsequently obtained via multiplying the load and deformation of samples. The incident energy is constant in the current investigation, and the bigger the load capacity, the smaller the deformation; hence, the deformation reduces with the dip angle varying from 0 to 75°.

Figure 11 presents the peak load comparison under static and dynamic conditions. As the crack dip angle increases, the peak load increases. Under static loading, both the peak load and growth rate are obviously lower than those under dynamic loading. The peak load increases slowly for both static and dynamic loading when the dip angle is between 0° and 30°, while it increases dramatically at $\theta > 30°$.

Figure 12 indicates the relationship between peak load and crack dip angle of samples at various concrete strengths. The peak load increases gently when the dip angle varies from 0° to 30°, and after 30°, it increases significantly as the dip angle increases. The above results indicate that the peak load is obviously impacted by the dip angle θ. In addition, it is demonstrated that the whole strength of the sample is greatly influenced by the increase in concrete strength. Previous studies [59] indicate that the interface tensile strength is closely related to the cohesion between rock and concrete. An increase in concrete strength for rock–concrete structures leads to fewer pores at the interface and stronger bonding effect, which sequentially affects the mechanical properties (such as the cohesion) of rock–concrete interface. Additionally, there are many hydration products on the interface surface, which can improve the bonding performance of rock–concrete interface,

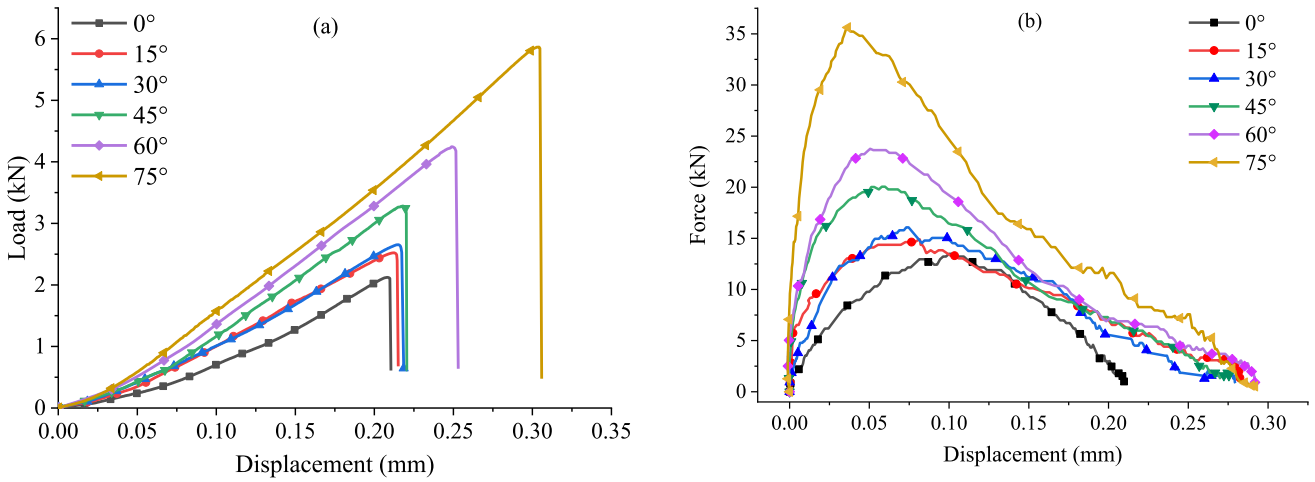

Fig. 10 Load–displacement curves of SCB samples

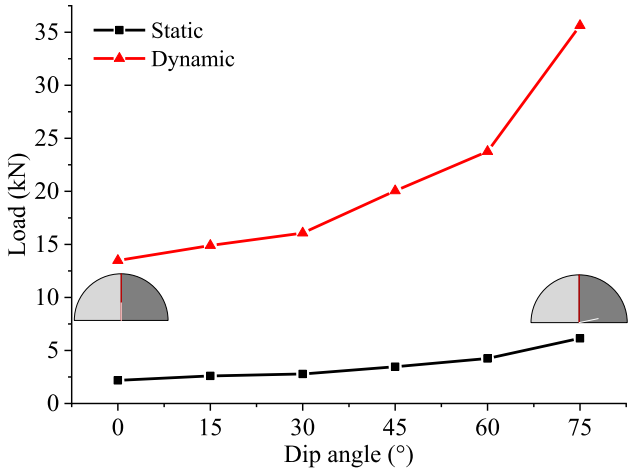

Fig. 11 Comparison of peak loads

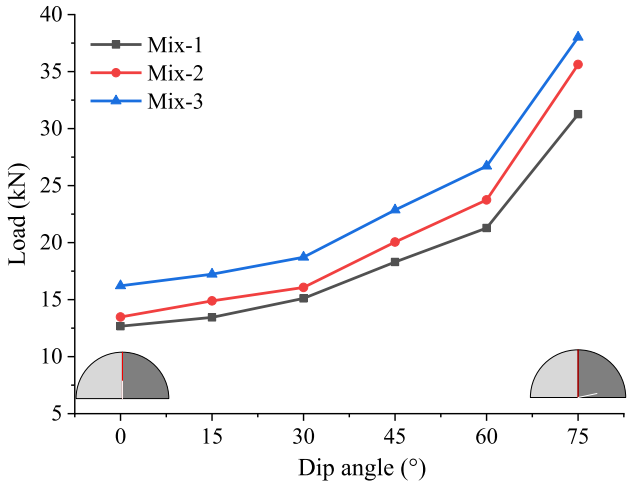

Fig. 12 Effects of dip angle on peak load of SCB samples at different concrete strength

thereby increasing the nominal tensile strength of rock–concrete sample. Figure 12 presents that the peak load of sample increases with increasing concrete strength, indicating that the increase of concrete strength can enhance the bonding force between rock and concrete. In our previous studies [57], it was found that the peak load significantly increases with increasing interface strength. The peak load tends to stabilize when the interface strength increases to a certain value. As interface strength increases, the difference in peak load between various dip angles increases.

4 Establish finite-element model

4.1 Calculation principle

Fracture toughness is frequently applied in evaluating the rock/concrete fracture resistance, which can be determined by the dimensionless stress intensity factor (SIF) and the critical load. For the SCB tests, the mode I and mode II SIFs in the static and dynamic case (samples satisfy the dynamic equilibrium under dynamic loading) can be expressed as follows [48, 49, 60]:

$$K_{\mathrm{I}}^{s,d} = \frac{P\sqrt{\pi a}}{2RB} Y_{\mathrm{I}}\left(\frac{a}{R}, \frac{S}{R}\right) \tag{4}$$

$$K_{\mathrm{II}}^{s,d} = \frac{P\sqrt{\pi a}}{2RB} Y_{\mathrm{II}}\left(\frac{a}{R}, \frac{S}{R}\right), \tag{5}$$

where $K_{\mathrm{I}}^{s,d}$ and $K_{\mathrm{II}}^{s,d}$ represent mode I and mode II SIFs under both static and dynamic loading conditions, respectively, P refers to loading force, R and B refer to radius and thickness of SCB sample, respectively, and Y_{I} and Y_{II} are the mode I and mode II dimensionless SIFs, both of which can be determined through finite-element approach.

Mixed mode I–II SIF K_{eff} is generally referred to as the effective SIF, which reflects the fracture characteristics under the mixed-loading mode and is defined below [61]

$$K_{\mathrm{eff}}^{s,d} = \sqrt{(K_{\mathrm{I}}^{s,d})^2 + (K_{\mathrm{II}}^{s,d})^2}. \tag{6}$$

In addition, the mixed parameter M^e can be introduced to discuss the mechanical characteristics under various loading conditions, which is described below

$$M^e = \frac{2}{\pi} \tan^{-1}\left(\frac{K_{\mathrm{I}}}{K_{\mathrm{II}}}\right). \tag{7}$$

The material is in mode I loading when $K_{\mathrm{II}}=0$, $M^e=1$, and it is in mode II loading if $K_{\mathrm{I}}=0$, $M^e=0$. Various mode mixity ratios ($M^e = 1, (0-1)$ and 0) are determined via adjusting the dip angle of pre-existing crack.

The elastic theory of interfacial fracture of dissimilar materials serves as a theoretical foundation for the current study, which uses finite-element software to determine the SIF using the J-integral approach. For the interfacial fracture in the case of plain strain, the correlation between stresses and SIFs of the crack tip at interface of two dissimilar materials can be determined as follows [12]:

$$\sigma_{22} + i\sigma_{12} = \frac{(K_I + iK_{\mathrm{II}})r^{i\varepsilon}}{\sqrt{2\pi r}}, \tag{8}$$

where $i = \sqrt{-1}$ and ε represent the oscillation index, and

$$\varepsilon = \frac{1}{2\pi} \ln\left(\frac{1-\beta}{1+\beta}\right), \tag{9}$$

where β denotes a Dundurs' parameter

$$\beta = \frac{1}{2}\frac{G_A(1-2\nu_B) - G_B(1-2\nu_A)}{G_A(1-2\nu_B) + G_B(1-2\nu_A)}, \tag{10}$$

where G denotes shear modulus and v refers to Poisson's ratio. Subscripts A and B denote material A and B, respectively.

The energy release rate and SIFs are related, which is described as the following formula:

$$G = \frac{1}{2}\left(1-\beta^2\right)\left[\frac{1-\nu_A^2}{E_A} + \frac{1-\nu_B^2}{E_B}\right]|K|^2 \tag{11}$$

$$|K| = \sqrt{K_{\mathrm{I}}^2 + K_{\mathrm{II}}^2}. \tag{12}$$

4.2 Computation and analysis of SIF

Figure 13 presents the numerical model developed by the ABAQUS software for solving SIFs of SCB samples. The geometric size of the numerical model of the sample corresponds to that of test sample. There are 19,986 elements and 60,609 nodes in the mesh, with refinement of the mesh in crack tip region. The J-integral method is used as a calculation principle to determine the SIF of the crack tip. Five contours are distributed from inside to outside in the crack tip region, and the SIF of fifth contour is utilized in this study.

The results obtained in this study are compared with those of the isotropic SCB sample proposed by Lim et al. [60]. Mode I stress intensity factors with different a/R are compared in Table 3. The calculation results in the study are generally in accordance with those of Lim et al. [60].

Table 3 Comparison for SIFs

a/R	S/R	Present K_{I}	K_{I} in [60]	Error/%
0.1	0.5	2.763	2.76	0.11
0.3	0.5	2.578	2.573	0.19
0.5	0.5	3.611	3.603	0.22
0.67	0.5	6.328	6.315	0.21
0.8	0.5	12.965	12.93	0.27

The impacts of a/R, θ, and $E_{\mathrm{B}}/E_{\mathrm{A}}$ on dimensionless SIF (Y_{I} and Y_{II}) are depicted in Fig. 14a and b illustrate that for a given crack length ratio, Y_{I} first decreases and subsequently increases as θ increases, while Y_{II} increases first and then decreases as θ increases. Additionally, at lower or larger dip angles, the absolute value of Y_{I} increases significantly with increasing the crack length ratio. When $\theta > 30°$, Y_{I} is lower than 0 and Y_{II} changes irregularly, which is due to the additional traction caused by friction along crack face after closure of pre-cracked. As illustrated in Fig. 14c and d, Y_{I} and Y_{II} increase as the modulus ratio increases. When $\theta = 45°$ approximately, $Y_{\mathrm{I}} = 0$, the shear stress is largest, that is, pure-mode II fracture occurs. Furthermore, Fig. 14d presents that Y_{II} reaches its maximum value at a dip angle of about 31°, suggesting that pure-mode II fracture is not based on the maximum of Y_{II}. Figure 14b and d presents that Y_{II} of layered material is not 0 under mode I loading, which is different from that of single material, indicating that the material difference of the layered material has a significant influence on Y_{I} and Y_{II} at the tip of crack.

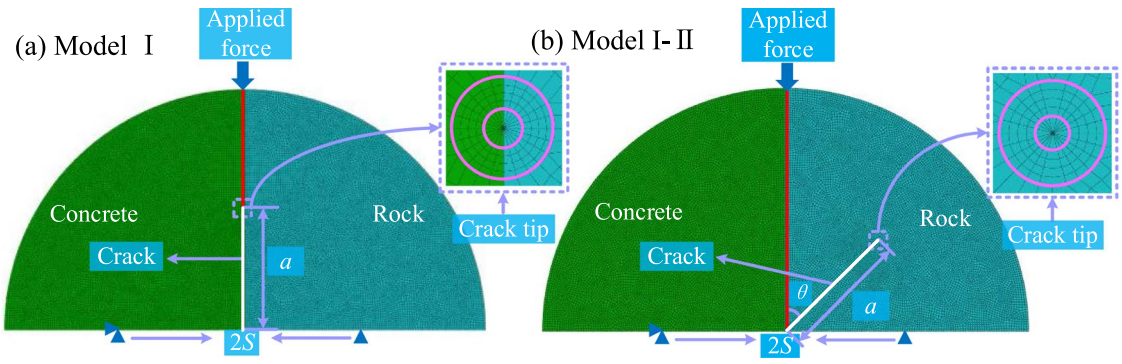

Fig. 13 Calculation model for SIF: **a** Model I and **b** Model I–II

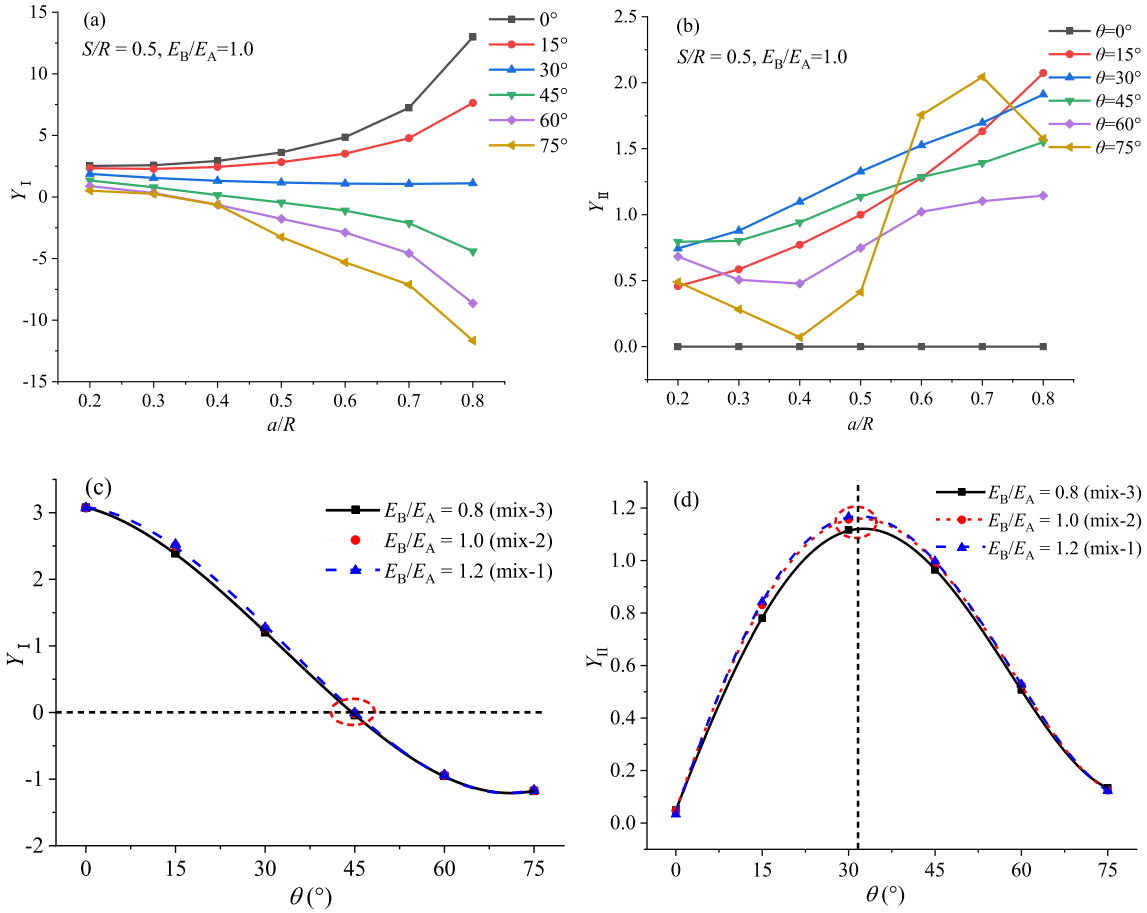

Fig. 14 Effects of θ and E_B/E_A on normalized SIFs: **a** Y_I versus θ, **b** Y_{II} versus θ, **c** Y_I versus E_B/E_A, and **d** Y_{II} versus E_B/E_A

5 Fracture toughness analysis and discussion

5.1 Static fracture toughness

The effect of dip angle on static fracture toughness (K^s_{Ic}, K^s_{IIc} and K^s_{effc}) for different concrete strength is shown in Fig. 15. It is observed from Fig. 15a and b that the static fracture toughness varies nonlinearly with increasing crack dip angle, and mode I static fracture toughness K^s_{Ic} reduces with an increase in dip angle at $\theta < 45°$, but increases with increasing the dip angle at $\theta \geq 45°$. Moreover, mode II static fracture toughness K^s_{IIc} shows a contrary trend when $\theta < 45°$ and $\theta \geq 45°$. Notably, Fig. 15a presents that the change rate of K^s_{Ic} is small for lower dip angles ($\theta \leq 15°$). Figure 15b shows that the change rate of K^s_{IIc} is large for lower and higher dip angles ($\theta \leq 15°$ and $\theta \geq 60°$), while if $15° < \theta < 60°$. The change rate of K^s_{IIc} shows an inverted U-shaped change. As illustrated in Fig. 15c, the static mixed fracture toughness K^s_{effc} initially reduces and subsequently increases with an increase in dip angle, while when $\theta = 45°$, it is at its lowest. It is because mode II fracture occurs at $\theta = 45°$. Additionally, K^s_{Ic}, K^s_{IIc}, and K^s_{effc} can be enhanced by increasing concrete strength. This is because the increase in concrete strength leads to the increase of interface cohesion, which results in higher loads required for sample fracture.

5.2 Dynamic fracture toughness

The impact of dip angle on dynamic fracture toughness (K^d_{Ic}, K^d_{IIc}, and K^d_{effc}) for different concrete strength is shown in Fig. 16. As demonstrated in Figs. 15 and 16, static and dynamic fracture toughness varies similarly. Moreover, the study suggests that dynamic fracture toughness improves with an increase in concrete strength.

Figure 17 depicts the correlation between static and dynamic fracture toughness at different dip angles. As shown in Fig. 17a, K^s_{Ic} and K^d_{Ic} vary similarly with dip angle, while K^d_{Ic} varies more significantly. The overall trend of the difference between K^s_{Ic} and K^d_{Ic} reduces initially and subsequently increases with increasing dip angle. If the dip angle is low or high ($\theta = 0°$ or $\theta = 75°$), the difference between K^s_{Ic} and K^d_{Ic} is larger, which are 3.46 MPa·m$^{1/2}$ and 3.44 MPa·m$^{1/2}$ separately, that is, K^d_{Ic} is about six times K^s_{Ic}. When $\theta = 45°$,

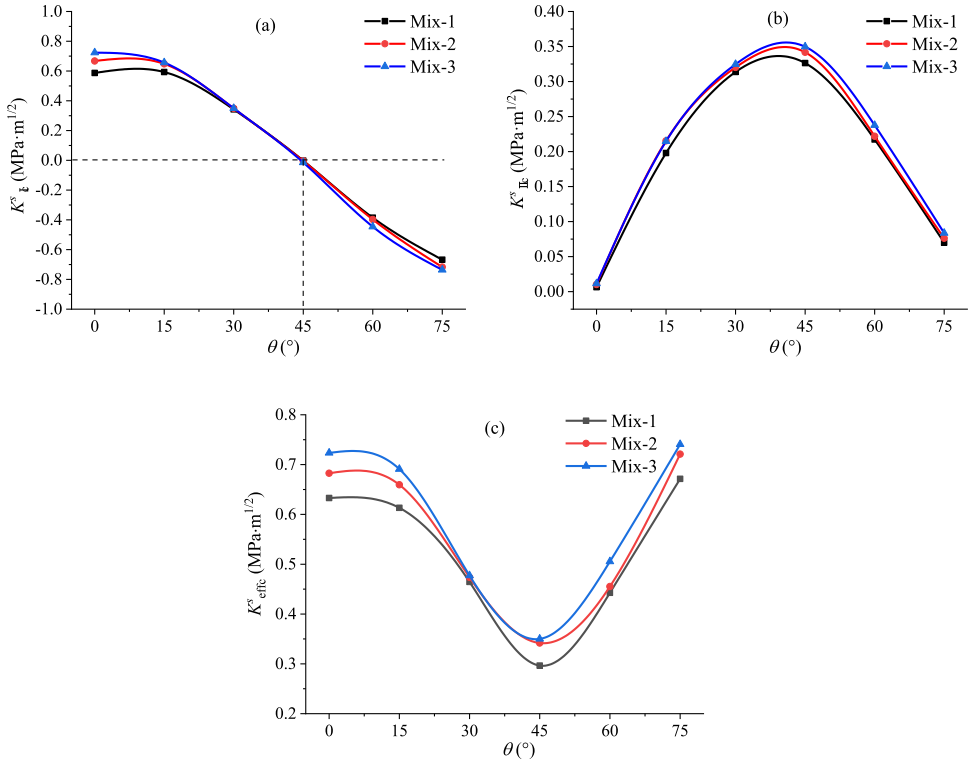

Fig. 15 Impacts of dip angle on fracture toughness: **a** K^s_{Ic}, **b** K^s_{IIc}, and **c** K^s_{effc}

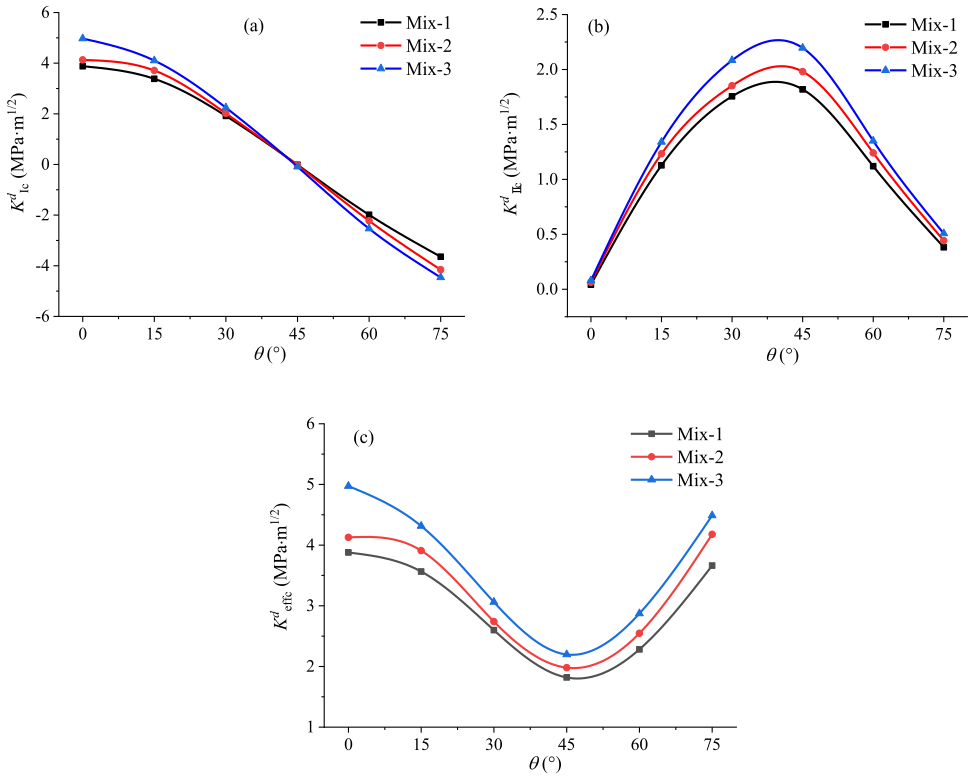

Fig. 16 Influences of dip angle on dynamic fracture toughness for different concrete strength: **a** K^d_{Ic}, **b** K^d_{IIc}, and **c** K^d_{effc}

the difference between K^s_{Ic} and K^d_{Ic} is basically 0, explaining the dominance of mode II fracture. This is because the mode I fracture toughness K^s_{Ic} and K^d_{Ic} is 0 at $\theta = 45°$.

Figure 17b presents that the difference between K^s_{IIc} and K^d_{IIc} increases first and reduces subsequently with increasing dip angle. The difference between K^s_{IIc} and

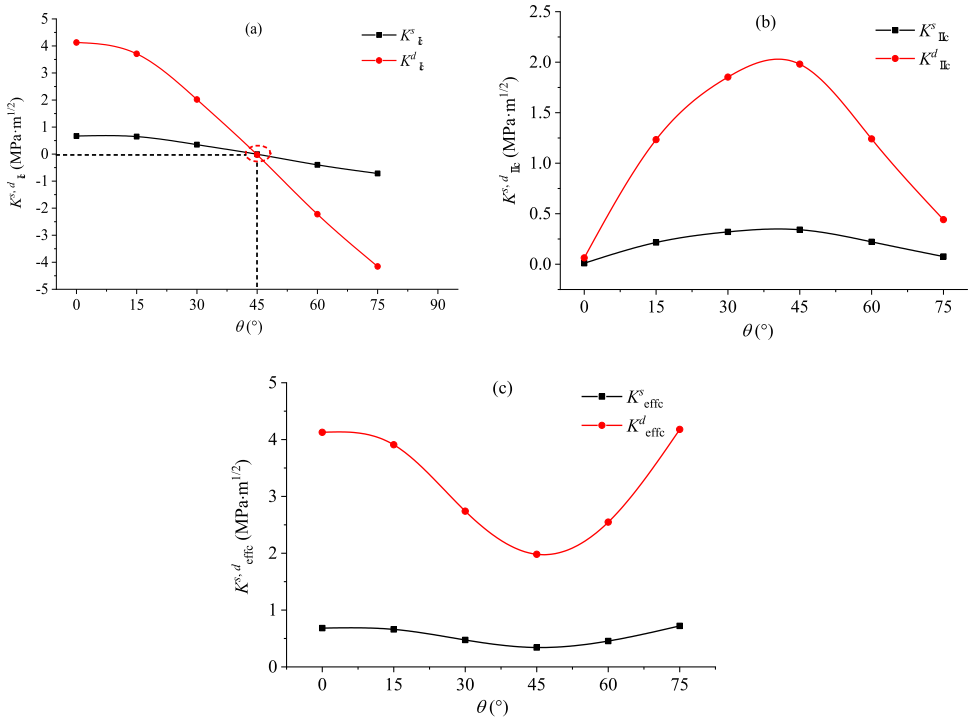

Fig. 17 The variations in fracture toughness at various dip angles: **a** $K^{s,d}_{Ic}$, **b** $K^{s,d}_{IIc}$, and **c** $K^{s,d}_{effc}$

K^d_{IIc} is 0.05 MPa·m$^{1/2}$ at $\theta=0°$, while when the dip angle approaches 40°, it increases to 1.64 MPa·m$^{1/2}$. For $\theta=90°$, the difference between K^s_{IIc} and K^d_{IIc} is 0.36 MPa·m$^{1/2}$. The results reveal that the difference between K^s_{IIc} and K^d_{IIc} is larger at medium dip angles. This is because mode I fracture mainly occurs when θ is small or large.

The comparison of K^s_{effc} and K^d_{effc} at various dip angles is indicated in Fig. 17c. The difference between K^s_{effc} and K^d_{effc} is 3.45 MPa·m$^{1/2}$ at $\theta=0°$, 1.64 MPa·m$^{1/2}$ when $\theta=45°$, and 3.46 MPa·m$^{1/2}$ when θ is further increased to 75°. This is due to the weak interfacial bonding, which causes tensile fracture along the interface at $\theta=0°$ (loading along the interface). Shear fracture appears primarily in samples for $\theta=45°$, while combined compression–shear failure occurs for $\theta=75°$. The above results indicate that dip angle plays an important role in determining the disparities between static and dynamic fracture toughness, and the latter of which is more reliant on dip angle than the former.

5.3 Effects of various factors on fracture resistance

The relationship between $K^{s,d}_{Ic}$ and $K^{s,d}_{IIc}$ is illustrated in Fig. 18. It is observed in Fig. 18a and b that the variations of $K^{s,d}_{Ic}$ and $K^{s,d}_{IIc}$ are similar, both of which are semi-ellipse, and the curves of $K^{s,d}_{Ic}$ and $K^{s,d}_{IIc}$ gradually expand outward with increasing concrete strength, indicating that the increase in concrete strength has a strengthening impact on crack resistance of sample.

The static and dynamic modal mixing ratio $K^{s,d}_{IIc}/K^{s,d}_{Ic}$ characterizes the correlation between tensile stress and shear stress [62]. All combinations of $K^{s,d}_{Ic}$ and $K^{s,d}_{IIc}$ form an envelope, reflecting the fracture characteristics of samples under various compositions of tensile and shear stresses. It can be concluded that the higher the $K^{s,d}_{IIc}/K^{s,d}_{Ic}$, the higher the ratio of $K^{s,d}_{IIc}$, indicating that the shear fracture is more prone to appear. Figure 18c indicates the impact of various concrete strengths and θ on the modal mixing ratio $K^{s,d}_{IIc}/K^{s,d}_{Ic}$. The results show that $K^{s,d}_{IIc}/K^{s,d}_{Ic}$ is the largest when $\theta=45°$. This is because the sample mainly undergoes slip failure (mode II fracture) at $\theta=45°$. The proportion of $K^{s,d}_{IIc}/K^{s,d}_{Ic}$ is larger at $30°<\theta<60°$, and it increases first and decreases subsequently with an increase in θ, showing that the mode II fracture toughness is greater in the medium dip angle range, that is, shear failure mainly occurs.

The fracture toughness ratio (K_{effc}/K_{Ic}) characterizes the fracture resistance and reflects the cracking behavior of the sample. For the purpose of investigating the fracture resistance of rock–concrete composites with different concrete strengths, the mixing parameters M^e of different crack dip angles are determined based on Eqs. (4), (5) and (7). The material undergoes pure-mode I failure when $M^e=1$, and it undergoes pure-mode II failure for $M^e=0$. If $0<M^e<1$, mixed-mode I-II fracture occurs. The relationship between K_{effc}/K_{Ic} and M^e of layered SCB samples for different concrete strength is presented in Fig. 19. This study indicates that as the modal mixing parameter M^e decreases and moves from mode I to mode II, and K_{effc}/K_{Ic} is significantly weakened. This is because of the sample fracture from mode I to mode II, resulting in a decrease in the proportion of mode I fracture toughness and an increase in mode II fracture

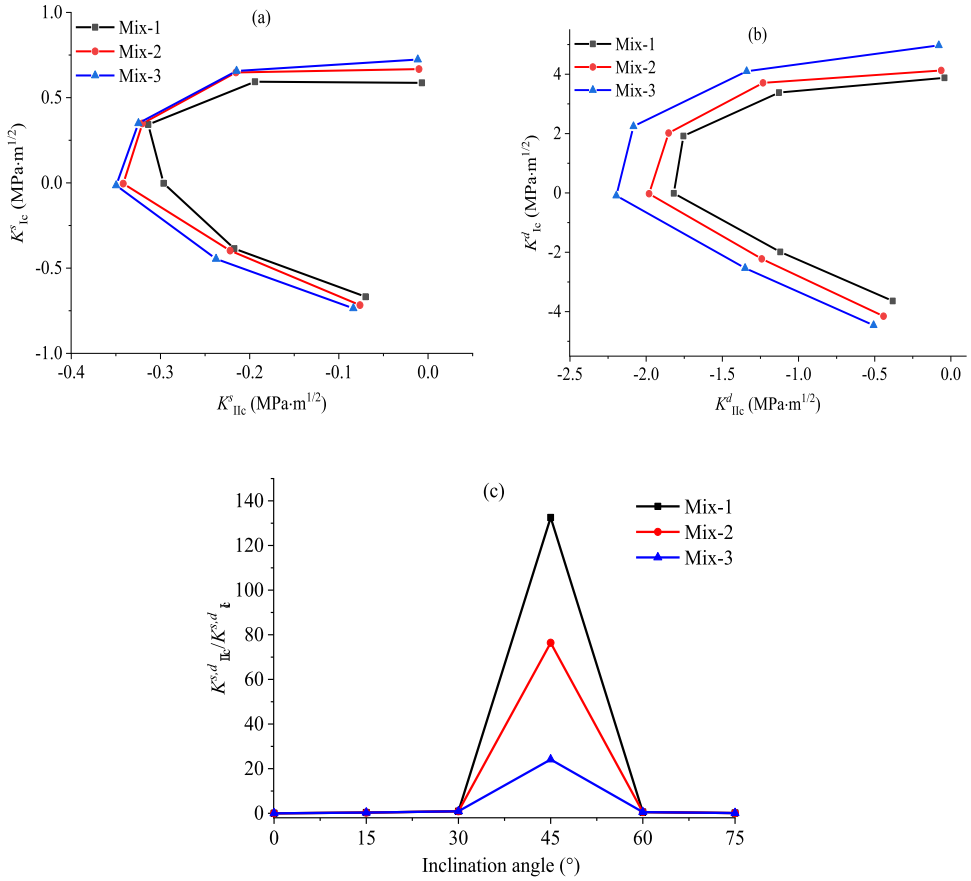

Fig. 18 Correlation between $K^{s,d}_{Ic}$ and $K^{s,d}_{IIc}$: **a** K^s_{Ic} versus K^s_{IIc}, **b** K^d_{Ic} versus K^d_{IIc}, and **c** $K^{s,d}_{IIc}/K^{s,d}_{Ic}$ versus θ

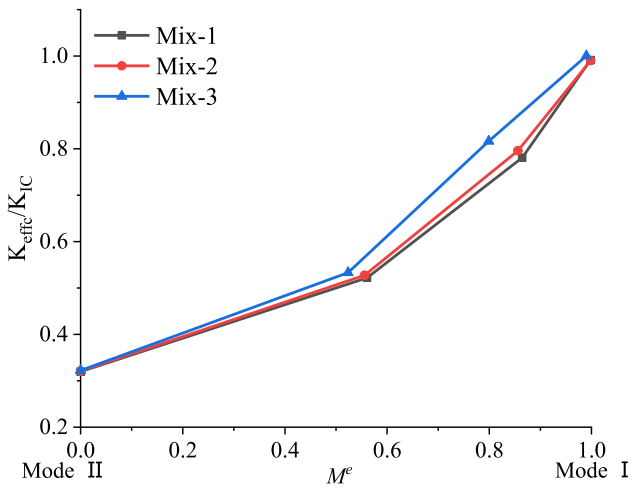

Fig. 19 Influence of concrete strength on fracture resistance (K_{effc}/K_{Ic})

toughness. The sample is prone to slip failure, and the presence of interface and crack also weakens its bearing capacity. The investigation carried out by Lim et al. [60] reveals similar results. Furthermore, Fig. 19 shows that an increase in concrete strength has a strengthening effect on K_{effc}/K_{Ic}, indicating that the fracture resistance of layered structures is improved via increasing the concrete strength.

6 Summary and conclusions

The fracture characteristics of rock-based layered materials were carefully investigated via static and dynamic SCB experiments. The impacts of various crack dip angles and concrete strength on fracture mode and fracture toughness were discussed. The main conclusions were summarized:

1. Three fracture modes can be classified under static and dynamic loading: interfacial/tensile fracture, combined tensile–shear fracture, and combined compression–shear fracture. The crack dip angle θ plays a critical role in the formation of fracture modes. When $\theta = 0°$, interface fracture mainly occurs in the layered SCB samples, and the fracture mode changes to combined tensile–shear fracture when $\theta = 15°$, 30°, and 45°, and combined compression–shear fracture occurs when θ further increases to 60° and 75°.
2. Under dynamic loading, the strength of concrete is highly connected to secondary cracks, and the decrease in concrete strength will induce an increase in the number of secondary cracks. The crack dip angle plays a controlling role in the fracture expansion path of layered SCB samples regardless of static or dynamic loading. With increasing dip angle, the angle of wing crack with

respect to the interface initially increases and subsequently reduces. When $\theta > 45°$, the pre-existing crack closes, and new cracks are not opening anymore from the crack tip. Additionally, the crack dip angle and concrete strength have a strengthening effect on the peak load.

3. Y_I and Y_{II} present significant dependence on dip angle and modulus ratio. Under mode I loading, Y_{II} of layered material is not 0, indicating that the material difference of layered material has an essential effect on Y_I and Y_{II} of the composite crack tip. If θ is about 45°, pure-mode II fracture occurs. The $K^{s,d}{}_{Ic}$ and $K^{s,d}{}_{IIc}$ turn around at $\theta = 45°$ and 40°, respectively, and the $K^{s}{}_{effc}$ and $K^{d}{}_{effc}$ increase as θ increases. The θ plays a vital role in controlling the disparity between static and dynamic fracture toughness, and the latter of which depends more strongly on the dip angle θ than the former. Further analysis indicated that the static and dynamic modal mixing ratio $K^{s,d}{}_{IIc}/K^{s,d}{}_{Ic}$ turns around at a dip angle of 45°, and it increases initially and subsequently decreases with an increase in dip angle θ. As the modal mixing parameter M^e decreases and moves from mode I to mode II, and K_{effc}/K_{Ic} is obviously weakened. Furthermore, the increase in concrete strength results in a strengthening impact on the cracking behavior of rock-based layered structures.

Acknowledgements The work is fully supported by National Natural Science Foundation of China (51974360, 52274106). The authors are very grateful to the financial contribution and convey their appreciation for supporting this basic study.

Data availability The data that support the findings of this study are available from the corresponding author upon reasonable request.

Declarations

Conflict of interest All authors declare that there are no known competing financial interests or personal relationships that could have appeared to influence the work reported in this paper.

Ethical approval This article does not contain any studies with human participants or animals performed by any of the authors.

References

1. Barrett SVL, McCreath DR. Shotcrete support design in blocky ground: towards a deterministic approach. Tunn Undergr Space Technol. 1995;10(1):79–89.
2. Lam TSK, Johnston IW. Shear behaviour of regular triangular concrete/rock joints—analysis. J Geotech Eng Div ASCE. 1989;115(5):711–27.
3. Ulfberg A, Gonzalez-Libreros J, Das O, Bista D, Westberg Wilde M, Johansson F, et al. Probabilistic finite element analysis of failures in concrete dams with large asperities in the rock–concrete interface. Arch Civ Mech Eng. 2023;23(2):109.
4. Fishman YA. Features of shear failure of brittle materials and concrete structures on rock foundations. Int J Rock Mech Min Sci. 2008;45(6):976–92.
5. Alneasan M, Behnia M, Bagherpour R. Analytical investigations of interface crack growth between two dissimilar rock layers under compression and tension. Eng Geol. 2019;259:105–88.
6. Huang S, Yan E, Fang K, Li X. Effects of binder type and dosage on the mode I fracture toughness of cemented paste backfill-related structures. Constr Build Mater. 2021;270: 121854.
7. Sujatha V, Kishen JMC. Energy release rate due to friction at bi-material interface in dams. J Eng Mech. 2003;129:793–800.
8. Fishman YA. Stability of concrete retaining structures and their interface with rock foundations. Int J Rock Mech Min Sci. 2009;46(6):957–66.
9. Zhang AB, Wang BL. An opportunistic analysis of the interface crack based on the modified interface dislocation method. Int J Solids Struct. 2013;50(1):15–20.
10. Dang H, Zhao M, Fan C, Chen Z. Extended displacement discontinuity method for an interface crack in a three-dimensional transversely isotropic piezothermoelastic bi-material. Part 2: numerical method. Int J Solids Struct. 2017;109:199–209.
11. Zhou L, Zhu Z, Dong Y, Niu C. Investigation of dynamic fracture properties of multi-crack tunnel samples under impact loads. Theor Appl Fract Mech. 2020;109: 102733.
12. Wang X, Zhu Z, Zhou L, Ma L, Zhou C, Wang Z, et al. Study on the effects of joints orientation and strength on failure behavior in shale specimen under impact loads. Int J Impact Eng. 2022;163: 104162.
13. Meng Y, Jing H, Zhou Z, Zhang L, Sun S. Experimental investigation on the mixed-mode fracture behavior of rock-like material with bedding plane. Theor Appl Fract Mech. 2022;117: 103159.
14. Chang X, Zhang X, Cheng L, Fu L. Crack path at bedding planes of cracked layered rocks. J Struct Geol. 2022;154: 104504.
15. Tambat A, Subbarayan G. Simulations of arbitrary crack path deflection at a material interface in layered structures. Eng Fract Mech. 2015;141:124–39.
16. Luo S, Gong F. Linear energy storage and dissipation laws during rock fracture under three-point flexural loading. Eng Fract Mech. 2020;234: 107102.
17. Marsavina L, Sadowski T, Knec M. Crack propagation paths in four point bend Aluminium—PMMA specimens. Eng Fract Mech. 2013;108:139–51.
18. Charalambides PG, Lund J, Evans AG, McMeeking RM. A test specimen for determining the fracture resistance of bi-material interfaces. Int J Appl Mech. 1989;56:77–82.
19. Suo Z, Hutchinson JW. Sandwich test specimens for measuring interface crack toughness. Mat Sci Eng. 1989;107:135–43.
20. Myong Lee K, Buyukozturk O, Oumera A. Fracture analysis of mortar-aggregate interfaces in concrete. J Eng Mech. 1992;118(10):2031–46.
21. Buyukozturk O, Hearing B. Crack propagation in concrete composites influenced by interface fracture parameters. Int J Solids Struct. 1998;35:4055–66.
22. Agrawal A, Karlsson AM. On the reference length and mode mixity for a bi-material interface. ASME J Eng Mater Technol. 2007;129:580–7.
23. Yang SC, Li S, Li Z, Huang S. Experimental investigation on fracture toughness of interface crack for rock/concrete. Int J Modern Phys B. 2008;22:6141–8.
24. Zhong H, Ooi ET, Song C, Ding T, Lin G, Li H, et al. Experimental and numerical study of the dependency of interface fracture in concrete–rock specimens on mode mixity. Eng Fract Mech. 2014;124–125:287–309.

25. Chen Y, Hu Y, Hu X. Quasi-brittle fracture analysis of large and small wedge splitting concrete specimens with size from 150 mm to 2 m and aggregates from 10 to 100 mm. Theor Appl Fract Mech. 2022;121: 103474.
26. Guan J, Yuan P, Li L, Yao X, Zhang Y, Meng W. Rock fracture with statistical determination of fictitious crack growth. Theor Appl Fract Mech. 2021;112: 102895.
27. Guan J, Zhang Y, Meng J, Yao X, Li L, He S. A simple method for determining independent fracture toughness and tensile strength of rock. Int J Min Sci Technol. 2022;32(4):707–26.
28. Guan J, Yin Y, Li Y, Yao X, Li L. A design method for determining fracture toughness and tensile strength pertinent to concrete sieving curve. Eng Fract Mech. 2022;271: 108596.
29. Dong W, Wu Z, Zhou X. Fracture mechanisms of rock–concrete interface: experimental and numerical. J Eng Mech. 2016;142(7):04016040.
30. Dong W, Yang D, Zhang B, Wu Z. Rock-concrete interfacial crack propagation under mixed mode I–II fracture. J Eng Mech. 2018;144(6):4018039.
31. Yuan W, Dong W, Zhang B, Zhong H. Investigations on fracture properties and analytical solutions of fracture parameters at rock–concrete interface. Constr Build Mater. 2021;300: 124040.
32. Kuruppu MD, Obara Y, Ayatollahi MR, Chong KP, Funatsu T. ISRM-suggested method for determining the mode I static fracture toughness using semi-circular bend specimen. Rock Mech Rock Eng. 2014;47:267–74.
33. Wang H, Zhao F, Huang Z, Yao Y, Yuan G. Experimental study of mode-I fracture toughness for layered shale based on two ISRM-suggested methods. Rock Mech Rock Eng. 2017;50:1933–9.
34. Dutler N, Nejati M, Valley B, Amann F, Molinari G. On the link between fracture toughness, tensile strength, and fracture process zone in anisotropic rocks. Eng Fract Mech. 2018;201:56–79.
35. Huang D, Li B, Ma W, Cen D, Song Y. Effects of bedding planes on fracture behavior of sandstone under semi-circular bending test. Theor Appl Fract Mech. 2020;108: 102625.
36. Nejati M, Aminzadeh A, Saar MO, Driesner T. Modified semi-circular bend test to determine the fracture toughness of anisotropic rocks. Eng Fract Mech. 2019;213:153–71.
37. Fang K, Yang J, Wang Y. Comparison of the mode I fracture toughness of different cemented paste backfill-related structures: effects of mixing recipe. Eng Fract Mech. 2022;270: 108579.
38. Fang K, Cui L. Experimental investigation of fiber content and length on curing time-dependent mode-I fracture behavior and properties of cemented paste backfill and implication to engineering design. Fatigue Fract Eng Mater Struct. 2022;45(11):3302–18.
39. Wang Y, Yang R. Study of the dynamic fracture characteristics of coal with a bedding structure based on the NSCB impact test. Eng Fract Mech. 2017;184:319–38.
40. Ju M, Li J, Li X, Zhao J. Fracture surface morphology of brittle geomaterials influenced by loading rate and grain size. Int J Impact Eng. 2019;133: 103363.
41. Liu Y, Fu A, Jiang B, Yu L, Wang X. Study on the static and dynamic fracturing properties of marble after being damaged dynamically. Adv Civ Eng. 2020;2020:1–13.
42. Wang W, Zhao Y, Teng T, Zhang C, Jiao Z. Influence of bedding planes on mode I and mixed-mode (I–II) dynamic fracture toughness of coal: analysis of experiments. Rock Mech Rock Eng. 2021;54(1):173–89.
43. Shi X, Zhao Y, Gong S, Wang W, Yao W. Co-effects of bedding planes and loading condition on mode-I fracture toughness of anisotropic rocks. Theor Appl Fract Mech. 2022;117: 103158.
44. Chang X, Zhang X, Qian LZ, Chen SH, Yu J. Influence of bedding anisotropy on the dynamic fracture behavior of layered phyllite. Eng Fract Mech. 2022;260: 108183.
45. Qiu H, Zhu Z, Wang M, Wang F, Ma Y, Lang L, et al. Study on crack dynamic propagation behavior and fracture toughness in rock-mortar interface of concrete. Eng Fract Mech. 2020;228: 106798.
46. Qiu H, Wang F, Zhu Z, Wang M, Yu D, Luo C, et al. Study on dynamic fracture behaviour and fracture toughness in rock-mortar interface under impact load. Compos Struct. 2021;271: 114174.
47. Sundaram BM, Tippur HV. Dynamics of crack penetration vs branching at a weak interface: an experimental study. J Mech Phys Solids. 2016;96:312–32.
48. Dai F, Xia K, Zheng H, Wang YX. Determination of dynamic rock mode-I fracture parameters using cracked chevron notched semi-circular bend specimen. Eng Fract Mech. 2011;78(15):2633–44.
49. Xia K, Huang S, Dai F. Evaluation of the frictional effect in dynamic notched semi-circular bend tests. Int J Rock Mech Min. 2013;62:148–51.
50. Xu Y, Dai F, Xu NW, Zhao T. Numerical Investigation of dynamic rock fracture toughness determination using a semi-circular bend specimen in split Hopkinson pressure bar testing. Rock Mech Rock Eng. 2016;49(3):731–45.
51. Li Y, Dai F, You W, Liu Y. An asymmetric semi-circular bend method for investigating fracture behavior of brittle rocks under dynamic mixed mode I/II loading. Rev Sci Instrum. 2021;92:35112.
52. Zhu Q, Li D, Han Z, Xiao P, Li B. Failure characteristics of brittle rock containing two rectangular holes under uniaxial compression and coupled static-dynamic loads. Acta Geotech. 2022;17:131–52.
53. Blaber J, Adair B, Antoniou A. Ncorr: open-source 2D digital image correlation Matlab software. Exp Mech. 2015;55:1105–22.
54. Pan B. Reliability-guided digital image correlation for image deformation measurement. Appl Optics. 2009;48(8):1535.
55. Dai F, Huang S, Xia K, Tan Z. Some fundamental issues in dynamic compression and tension tests of rocks using split Hopkinson pressure bar. Rock Mech Rock Eng. 2010;43:657–66.
56. Zukas JA, Nicholas T, Swift HF, Greszczuk LB, Curran DR. Impact dynamics. New York: Wiley; 1982.
57. Guo T, Liu K, Song R. Crack propagation characteristics and fracture toughness analysis of rock-based layered material with pre-existing crack under semi-circular bending. Theor Appl Fract Mech. 2022;119: 103295.
58. Chang X, Guo T, Zhang S. Cracking behaviours of layered specimen with an interface crack in Brazilian tests. Eng Fract Mech. 2020;228: 106904.
59. Zhu J, Bao W, Peng Q, Deng X. Influence of substrate properties and interfacial roughness on static and dynamic tensile behaviour of rock-shotcrete interface from macro and micro views. Int J Rock Mech Min Sci. 2020;132: 104350.
60. Lim IL, Johnston IW, Choi SK. Stress intensity factors for semi-circular specimens under three-point bending. Eng Fract Mech. 1993;44(3):363–82.
61. Ayatollahi MR, Aliha MRM. Fracture toughness study for a brittle rock subjected to mixed mode I/II loading. Int J Rock Mech Min Sci. 2007;44(4):617–24.
62. Hutchinson JW, Suo Z. Mixed-mode cracking in layered structures. Adv Appl Mech. 1991;29:64–191.